Dynamics of Bound Exciton Complexes in CdS Nanobelts

Xinlong Xu,[†] Yanyuan Zhao,[†] Edbert Jarvis Sie,[†] Yunhao Lu,[‡] Bo Liu,[†] Sandy Adhitia Ekahana,[†] Xiao Ju,[†] Qike Jiang,[§] Jianbo Wang,[§] Handong Sun,[†] Tze Chien Sum,[†,*] Cheng Hon Alfred Huan,[†] Yuan Ping Feng,[‡] and Qihua Xiong[†,⊥,*]

[†]Division of Physics and Applied Physics, School of Physical and Mathematical Sciences, Nanyang Technological University, Singapore 637371, [‡]Department of Physics, National University of Singapore, 2 Science Drive 3, Singapore 117542, [§]School of Physics and Technology, Center for Electron Microscopy and MOE Key Laboratory of Artificial Micro- and Nano-Structures, Wuhan University, Wuhan 430072, China, and [⊥]Division of Microelectronics, School of Electrical and Electronic Engineering, Nanyang Technological University, Singapore 639798

ABSTRACT Intrinsic defects such as vacancies, interstitials, and anti-sites often introduce rich luminescent properties in II–VI semiconductor nanomaterials. A clear understanding of the dynamics of the defect-related excitons is particularly important for the design and optimization of nanoscale optoelectronic devices. In this paper, low-temperature steady-state and time-resolved photoluminescence (PL) spectroscopies have been carried out to investigate the emission of cadmium sulfide (CdS) nanobelts that originates from the radiative recombination of excitons bound to neutral donors (I_2) and the spatially localized donor–acceptor pairs (DAP), in which the assignment is supported by first principle calculations. Our results verify that the shallow donors in CdS are contributed by sulfur vacancies while the acceptors are contributed by cadmium vacancies. At high excitation intensities, the DAP emission saturates and the PL is dominated by I_2 emission. Beyond a threshold power of approximately 5 μW, amplified spontaneous emission (ASE) of I_2 occurs. Further analysis shows that these intrinsic defects created long-lived (spin triplet) DAP trap states due to spin-polarized Cd vacancies which become saturated at intense carrier excitations.

KEYWORDS: CdS nanobelt · bound exciton complex · exciton interaction · ultrafast dynamics · defect level

Oxide and chalcogenide nanostructures show excellent electrical and optical properties. They offer rich platforms not only for the fundamental sciences[1–6] but also for optoelectronic applications, such as lasers,[7] solar cells,[8] field emitters and field-effect transistors,[9,10] and waveguides.[11] Recent reports of CdS-based exciton–plasmon interaction have further promoted the interests in CdS nanomaterials.[12] Unlike the quantum dot counterparts, in which surface states are the major defects, stoichiometric defects formed during synthesis are the majority of defects in nanowires and nanobelts.[4] These stoichiometric defects consist of sulfur (V_S) and cadmium (V_{Cd}) vacancies and interstitials such as Cd_I and S_I. In addition, anti-sites such as S_{Cd} and Cd_S are also possible. Such defects can trap electrons, holes, or excitons and form bound complexes. Fundamental physics becomes even more complicated and yet interesting if these bound complexes interact with each other as a function of population or temperature. Our research presented in this paper was motivated to understand the competing processes and the evolution of carrier dynamics following photoexcitation. A clear understanding of the mechanism and the nature of exciton dynamics in such nanobelts will facilitate further design, optimization, and development of nanobelt-based optoelectronic devices.

Temperature-dependent and time-resolved photoluminescence (PL) spectroscopy provides an essential probe to investigate the dynamic processes in nanostructures. Despite the numerous experimental studies of CdS nanocrystals and nanowires,[13,14] a thorough understanding of the exciton dynamics in CdS nanobelts is still lacking. This is manifested in the inconsistent PL peak identification in the existing literature.[15–20] For example, even though donor–acceptor pair (DAP) recombination was often assigned to the green emission band of unintentionally doped CdS PL spectra, the identification of the donor and acceptor is not clear. Such inconsistency actually prevails not only in CdS but also in many other II–VI semiconductor materials such as ZnO.[21,22] Although there was much effort to pin down such assignments in the 1970s (*e.g.*, the pioneering work by Hendry *et al.*,[23–26] Thomas and Hopfield,[27] and Christmann[28]), the intrinsic and extrinsic origins of these donors and acceptors remain controversial.

In the present study, we aim to probe the exciton dynamics in CdS nanobelts through varying the excitation power between the regions of spontaneous and amplified spontaneous emission (ASE). Comprehensive steady-state and transient spectroscopic studies as

* Address correspondence to tzechien@ntu.edu.sg, qihua@ntu.edu.sg.

Received for review December 22, 2010 and accepted March 30, 2011.

Published online March 30, 2011
10.1021/nn2008832

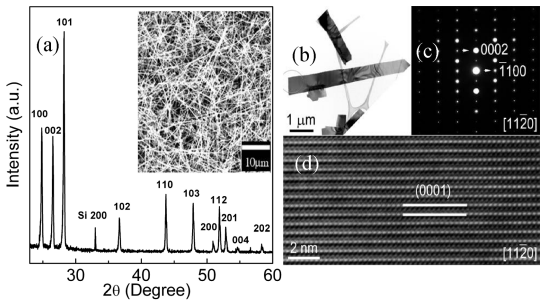

Figure 1. (a) X-ray diffraction spectrum of CdS nanobelts. The inset is an SEM image of as-grown CdS nanobelts on silicon substrate. (b) Low-magnification TEM image of CdS nanobelts. (c) Selected area electron diffraction pattern. (d) High-resolution TEM image of CdS nanobelts.

a function of pump fluence and temperature, supported by first principle calculations, allow us to reconstruct a clear picture of the origins of the excitons and their complicated recombination dynamics. The effects that influence such dynamics include (a) phonon-mediated effects and (b) multiexciton interactions such as Auger recombination and ASE processes. Supported by our theoretical calculations, we further identify that sulfur vacancies function as shallow donors while the cadmium vacancies dominate the acceptor level with a spin imbalance. Such spin polarization in turn gives rise to a much longer lifetime for the DAP compared to neutral donor bound excitons (I_2). Our study is significant to the understanding of defect-related emissions in CdS nanobelts and many other oxide and chalcogenide nanomaterials.

RESULTS AND DISCUSSION

Structural Characterization. CdS nanobelts were synthesized in a home-built vapor transport chemical vapor deposition (CVD) system.[16−18] X-ray diffraction (XRD) data shown in Figure 1a suggest that CdS belts exhibit wurtzite structure (JCPDS: 77-2306) with a good crystalline quality. Inset to Figure 1a shows an SEM image of the as-grown nanobelts. Figure 1b shows a typical low-magnification TEM image of CdS. It is noted that the length of nanobelts reaches several hundreds of micrometers and the thickness is on the scale of tens of nanometers, while the width is on the scale of tens of nanometers to micrometers. The selected area electron diffraction (SAED) pattern in Figure 1c also suggests a good crystalline quality. The high-resolution TEM (HRTEM) image in Figure 1d clearly indicates the two-dimensional lattice fringes consisting of (0001) and ($\bar{1}$100) planes, which reveals that the growth direction for the CdS nanobelts is perpendicular to the ($\bar{1}$100) plane.

From the point of view of the semiconductor band model, the ionic binding configuration of CdS is as follows: $Cd(3d^{10}4s^2) + S(3s^23p^4) \rightarrow Cd^{2+}(3d^{10}4s^0) + S^{2-}(3s^23p^6)$. Free electrons frequently occupy the lowest empty s-like level of the cations in the conduction band, while free holes in the valence band frequently arise from the highest occupied p-like level of the anions.[15,29,30] During synthesis, stoichiometric defects such as V_S, V_{Cd}, Cd_I, S_I, S_{Cd}, and Cd_S will be unintentionally formed, as vapor pressures for II and VI group elements are very different at certain temperatures.

Steady-State PL Spectroscopy. Figure 2a shows the room temperature PL and the diffuse reflectance spectra of our samples. The original diffuse reflectance data in Figure 2a have been converted to absorbance using the Kubelka−Munk equation[31] to allow us to directly observe the band gap and Urbach tail of CdS:[11]

$$f(R) = (1 - R)^2/(2R) = k/s \quad (1)$$

where R is the absolute reflectance of the original data, k is the molar absorption coefficient, and s is the scattering coefficient. The band gap at room temperature for our CdS nanobelts is approximately at 499 nm. The room temperature PL shows a strong emission at 508 nm. Thus, the Stokes shift is about 9 nm, approximately 44 meV, which is similar to that of the CdS nanocrystals with a radius of 1.0−2.3 nm.[32] PL in CdS nanocrystals originates not only from bright excitons but also from dark excitons as addressed by Yang *et al.*[33] Usually, a large Stokes shift with the value of ∼20−70 meV and long decay lifetimes suggest the presence of dark exciton states due to spin−orbit splitting.[32,34] Compared to quantum dots, the surface-to-volume ratio of nanobelts is smaller, which means that the surface effect due to dangling bonds in nanobelts is less significant than that in quantum dots. The full width at half-maximum (fwhm) in Figure 2a is ∼16.7 nm, which is much narrower than that in quantum dots. Quantum dots usually exhibit a fairly broad emission with a fwhm of more than 100 nm in the range of 450−700 nm,[14,35] due to a combination of the size dispersion and the surface effect.

To elucidate the origins of the emission, we have conducted temperature-dependent PL spectroscopy. When the temperature was decreased to approximately 150 K, an additional new broad band green emission appeared due to DAP (data not shown here). This is because bound excitons are formed readily at lower temperatures, favoring a DAP recombination. The activation energy k_BT = 12.9 meV, where k_B is the Boltzmann constant, is comparable with the donor binding energy (ranging from 5 to 50 meV) but smaller than the acceptor binding energy.[30] When the temperature was further decreased to 10 K, more emission features were resolved. Figure 2b shows a PL spectrum measured at 10 K and fitted with multiple Gaussian functions to determine the peak positions and width, where the peak intensity reflects the relative population of each species and the fwhm gives an indication of the energy spread of the population or lifetime of the photons.

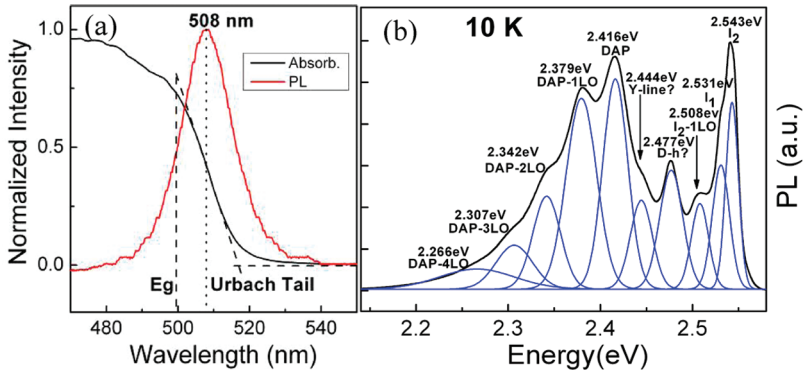

Figure 2. (a) Absorption spectroscopy, which is converted from original diffuse reflectance spectroscopy and PL spectroscopy at 300 K. The dashed lines indicate the Urbach tail and the band gap. (b) PL fine structure of CdS nanobelts at 10 K with a 325 nm He–Cd laser excitation. The blue curves are Gaussian line shape decompositions with each peak clearly labeled.

Due to the spin–orbit coupling and crystal-field interaction, the valence band in CdS splits into three sub-bands, giving rise to three exciton levels with characteristic energies of E_A = 2.550 eV, E_B = 2.568 eV, and E_C = 2.629 eV.[36–38] The first emission peak in our spectrum is located around 2.543 eV, which is close to the *A* exciton value, with a red shift of ~7 meV. This difference cannot be attributed to the nanostructure effect, which is usually blue-shifted when the size is reduced. In addition, our nanobelt size is too large to show any confinement effect.[4,39] Thomas and Hopfield found that in CdS platelets, in addition to intrinsic exciton lines, many lines are actually due to transitions involving bound excitons,[27,29] which are created when excitons bind to neutral/charged donors or acceptors. Recent experiments by Ip *et al.* on CdS nanobelts have shown a similar emission peak near 2.545 eV, and that was ascribed to originate from an exciton bound to a neutral donor.[16] Thus we ascribe the emission peak at 2.543 eV to neutral donor bound excitons, historically labeled as I_2.

The emission peak near 2.531 eV is weaker than I_2, and some groups have attributed this peak to I_1, referring to excitons bound to a neutral acceptor.[15,16,27] Reynolds *et al.* suggested that the intrinsic acceptor binding energy is much higher with an approximate value of 0.155 eV.[40] Our calculations for intrinsic acceptors also suggest that the intrinsic acceptor level is approximately 160 meV, which is higher than the value of 12 meV from Figure 2. Gutowski attributed this feature to arise from the extrinsic unintentional doping of Na acceptors.[41] Another possible cause is the phonon replica from low-frequency phonon modes such as the transverse acoustic mode (TA). However, studies on zone edge phonons in CdS are limited, and the amplitude of low-frequency phonon modes makes such assignment unreliable.[42,43] Hence, we tentatively attribute this peak to originate from extrinsic acceptor levels such as Na, which may be introduced as contaminants either from the source of CdS or handling during synthesis.

The peak at 2.508 eV, which locates just below I_2, was identified as the LO phonon replicas of I_2, with the emission of one longitudinal phonon (LO) (*i.e.*, I_2-1LO). The peak at 2.477 eV is approximately two LO phonons (*i.e.*, I_2-2LO) away from I_2, but it is stronger than I_2-1LO, which is unusual for the second-order phonon replica. Ekimov *et al.* observed a similar shape of the PL spectrum in CdS microcrystals and attributed this to holes that are bound to the donors (*i.e.*, D-h), but the original identification is inconclusive.[44] The 2.444 eV peak, which is weaker compared to the 2.416 eV peak, was previously attributed by Seto *et al.* to the Y-line that is characterized by a weak LO phonon coupling.[38] This emission arises mainly from excitons trapped at the structural defects and misfit dislocations near the heterointerface. On the other hand, Ekimov *et al.* attributed this peak to arise from electrons that are bound to the acceptor (*i.e.*, e-A). At this moment, we are unable to establish the origin of 2.444 eV emission.[44]

A series of peaks around 2.416 eV, which is followed by 2.379 and 2.342 eV, clearly demonstrate the characteristic multiple phonon replicas with an energy spacing of approximately one LO phonon (*i.e.*, 37 meV). Henry *et al.* first observed DAP sharp lines in CdS at 1.6 K, which is usually not very evident for II–VI semiconductors with wurtzite structure.[23] The sharpness of the line shape depends on the density of DAP, the distances between them, phonon broadening, and sample inhomogeneity. As stated by Moroz *et al.*, the electron–phonon couplings for excitons bound to impurities (I_2) are different from DAP–phonon coupling.[45] To demonstrate this, we calculate the Huang–Rhys factors from Figure 2 using the following function: $I_n = I_0 S^n/n!$, where I_n is the intensity of *n*-th order of phonon replica, I_0 is the zero phonon replica, and *S* is the Huang–Rhys factor.[46] Usually, the larger the *S* is, the stronger the exciton–phonon coupling is. The *S* values are approximately 0.9 and 0.6 for DAP and I_2, respectively, suggesting a stronger exciton–phonon coupling for DAP.

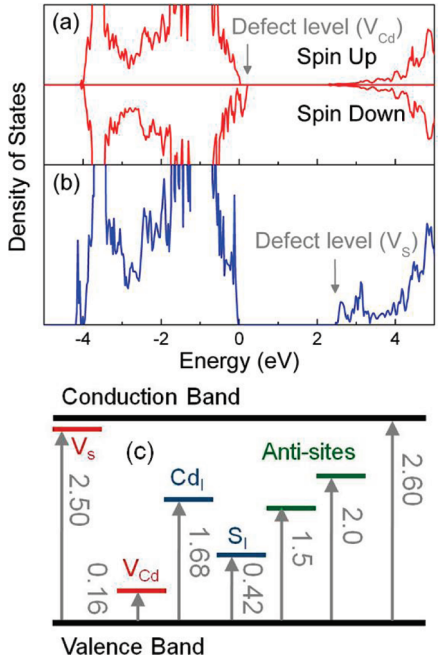

Figure 3. (a) Electronic density of states (DOS) of CdS with cadmium vacancy. The arrow indicates the spin imbalance. (b) Electronic DOS of CdS with sulfur vacancy. (c) Summary of the band diagram of CdS showing the intrinsic defect levels from the first principle calculation (units in eV).

Although there have been numerous reports on the features of DAP emission in CdS,[15,16,23,25,40,45,47] to our best knowledge, the chemical nature of the intrinsic donors and acceptors in native CdS still remains debatable. Sulfur vacancies have been suggested as the dominant donor-type defects, while cadmium vacancies have been proposed to be acceptor-type defects.[48] However, these claims were not backed up by strong experimental evidence and theoretical calculations.

First Principle Calculation. To further verify the origins of the I_2 and DAP peaks, we carried out first principle calculations using the Crystal package, which is a general purpose program for the study of crystalline solids based on the hybrid density functional method.[49] The optimized crystal parameters used in the calculation are listed in the following: CdS wurtzite structure with $a = b = 4.15$ Å and $c = 6.73$ Å. Defect calculations were performed using $3 \times 3 \times 2$ supercells corresponding to ~1.3% defect concentration, and $2 \times 2 \times 2$ k-point mesh was used for total energy calculations. The forces acting on the relaxed atoms are <0.02 eV/Å in the optimized structures. The intrinsic defects considered here are the sulfur vacancy, cadmium vacancy, interstitials, and anti-sites. Figure 3 shows a density of states (DOS) plot of CdS with cadmium (a) and sulfur (b) vacancies. Compared to sulfur vacancy, it is interesting to note that the defect level close to valence band maximum (VBM) is spin-polarized for cadmium vacancy with only spin-down DOS above the Fermi level. This suggests that the holes in the cadmium vacancies form acceptor levels which are spin-polarized. This spin polarization will strongly affect the DAP spontaneous emission rate as evidenced in our time-resolved PL measurements where the lifetimes of the DAPs (~300 ns) are at least 3 orders of magnitude longer compared to I_2 (~200 ps).

Figure 3c summarizes the energy levels of all intrinsic defects of interest obtained by the first principle method. On the basis of our calculations, it is concluded that the main contribution of the shallow donors comes from the sulfur vacancies with an energy E_D of approximate 100 meV, while the main contribution of the acceptors originates from the cadmium vacancies with E_A of approximately 160 meV. Comparing these values with our experimental data shown in Figure 2b, we conclude that the cadmium vacancy together with the sulfur donor level forms the DAP. The experimental value (2.416 eV) for DAP is in good agreement with the calculated value of ~2.34 eV. This small deviation may be attributed to the slight difference in the values of the band gap for the experiments (at 10 K) and that for the calculations (at 0 K). Our assignments based on first principle computation can explain some previous measurements. For example, Collins *et al.* suggested that sulfur vacancies were associated with the green edge emission.[50] It was also well-known that heating high conductivity CdS in excess sulfur resulted in an insulating crystal,[51] which was due to the annihilation of sulfur vacancies in excess sulfur atmosphere. One of the important findings by Christmann *et al.* using a mass spectrometer was that the rate of loss of Cd compared to S is much smaller when CdS platelets were heated and the sulfur vacancies dominate the surface depletion layer.[28] They also found that sulfur leaves the single-crystal CdS at temperature as low as 100 °C, creating a depletion layer mainly formed by sulfur vacancies. Sulfur vacancy is also a major source of surface defects in CdS nanocrystals.[35] The similarity in the spectral position as reported by many groups also favors the explanation in terms of the intrinsic effects.[16−18,52−54]

Other defects, such as Cd_I with an energy level of 1.68 eV above the valence band, S_I with 2.18 eV from the conduction band, and two anti-site defects with energy levels of 1.5 and 2.0 eV above the valence band, form the deep levels in CdS and contribute mainly to the red band luminescence which was observed by Yasuhiro *et al.* and was probably inaccurately attributed to cadmium interstitial.[55] Chen *et al.* also found that a cadmium-rich sample showed a peak centered around 2.07 eV,[56] which was attributed to sulfur vacancies, but based on our calculations, this peak could actually originate from the cadmium interstitials. Chen *et al.* also performed annealing under a cadmium atmosphere and reported a 1.48 eV emission, which likely arises from the anti-sites, in agreement with our calculations. It should be noted that there are several possible configurations for the anti-site defects, and

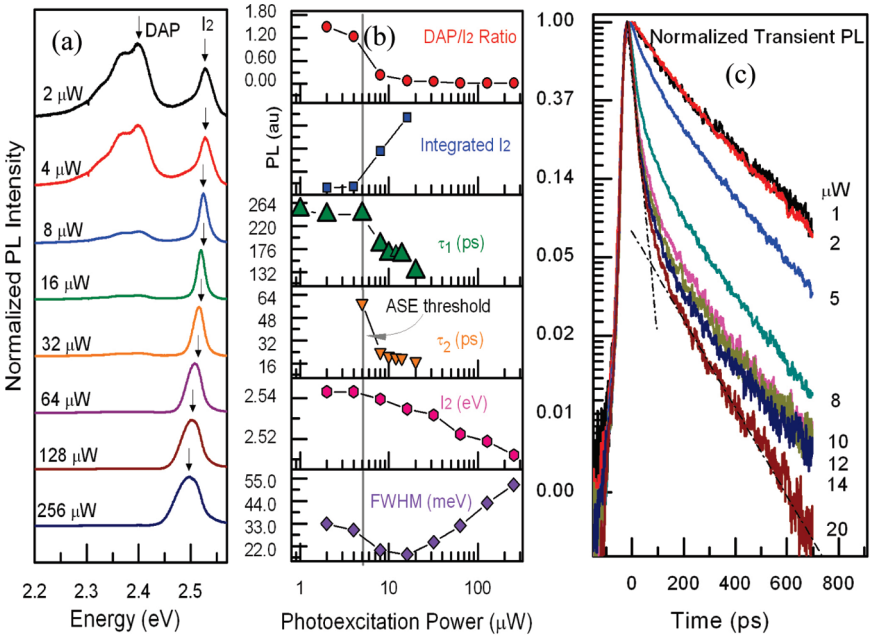

Figure 4. (a) Power-dependent PL spectra of CdS nanobelts at 10 K with 470 nm excitation (200 μm beam spot size). The arrows mark the center of the I_2 and DAP. (b) Relevant parameters as a dependence of pump power: (from top to bottom) DAP/I_2 ratio, integrated intensity of I_2, decay lifetimes (τ_1, τ_2), I_2 peak position, and fwhm of I_2. (c) Transient PL decay (normalized) of I_2 in CdS nanobelts at 10 K with pump power ranging from 1 to 20 μW. At low pump power, only one decay lifetime τ_1 was observed. As power increases further, a faster decay lifetime τ_2 due to multiexciton interactions appears as shown in (b).

the two examples shown in Figure 3c are the two most stable ones.

Pump-Power-Dependent Exciton Dynamics. The density of excitons plays a major role in the optical amplification of II–VI semiconductors. Magde *et al.* showed that, under intense illumination, an additional luminescence (slightly red-shifted from I_2) arises from an exciton–exciton interaction process, which was assigned to M band.[57] Nevertheless, little is known about how the excited species redistribute and interact among themselves. This interaction is important for nanolaser design and nanobelt-based waveguide applications. As we have also noted, the sulfur vacancies (donors) in our CdS nanobelts are abundant compared to the cadmium vacancies (acceptors). This suggests that the band-edge peak shown at high excitation intensity is dominated by the I_2 peak rather than the I_1 peak. For this reason, the characteristic PL features can be satisfactorily explained by the I_2 and the DAP emission processes.

Figure 4a shows the power-dependent PL spectra at 10 K with 470 nm excitation. The PL spectra were normalized with respect to the I_2 peak. Figure 4b summarizes various dependent variables of the PL features as a function of pump power (with a 200 μm laser spot size). Note that the DAP/I_2 intensity ratio drops drastically near 5 μW pump power. The saturation of DAP suggests that cadmium vacancy levels become fully populated as the pump threshold is approached. Beyond that threshold, the I_2 emission intensity undergoes a superlinear increase demonstrating ASE. The data beyond 16 μW were not plotted because a neutral density filter was used in order not to saturate the streak camera. ASE is defined as light that originates from a spontaneous emission, which is subsequently amplified by a stimulated emission. This process takes place in the absence of an optical cavity.[58] To support this assignment of ASE, we have also measured the transient dynamics of the I_2 emission, as shown in Figure 4c. As the excitation power approaches the threshold, an additional fast relaxation channel (τ_2) attributed to the ASE process is observed; the trend of its lifetime is also shown in Figure 4b, with both channels (τ_1 and τ_2) decreasing rapidly. We will discuss the transient behavior of these bound exciton complexes in more detail later.

ASE in II–VI semiconductor nanowires or nanobelts has been readily achieved with the threshold power density ranging from several μJ/cm^2 to tens of μJ/cm^2 depending on the quality of the sample.[59–63] Nevertheless, it is important to further address a few key questions. For instance, what is the mechanism and what are the levels involved in ASE? To a certain extent, we can provide a phenomenological explanation toward the ASE process from our calculation and our ensemble-averaged experiments. The basic criteria to achieve population inversion for ASE can be achieved by the three energy levels. In our CdS nanobelt system, the pumping levels are the quasi-continuum e–h pair states while the metastable level is the donor bound exciton state that gives rise to I_2 emission upon recombination to the ground state. ASE in quantum dots

with discrete levels can be achieved through the formation of biexcitons.[59,64] Unlike quantum dots, however, the nanobelt with its size much larger than its exciton Bohr radius will not change its electronic band structure appreciably. The abundant donor levels (V_S) and limited acceptor levels (V_{Cd}) mean that the I_2 emission dominates the DAP emission at high pump fluence. Multiple e−h pairs can be easily trapped at the donor levels under high pump fluence. Population inversion can occur readily at these donor levels, resulting in ASE. Unlike ASE, lasing usually manifests as a sharper threshold and especially the mode from cavities such as Fabry−Perot modes. A cavity (either formed as a natural cavity by crystal facets themselves or by mirror cavity) is needed for further lasing from the ASE process.

The population distribution of the donor bound exciton could also be traced from the peak position and the fwhm of I_2. First, the I_2 peak undergoes a red shift, as shown in Figure 4b, instead of a blue shift expected of the state-filling effect.[65] Although under high excitation power, a red shift can be induced by the exciton−exciton binding energy, the large carrier population also means that the carriers are subject to a highly screened Coulomb interaction, thus a red shift due to multiexcitonic binding energy is less likely.[66] This red shift is likely to originate from a local pump heating effect which introduces further phonon effect and renormalization of band structure. This can be further supported by the pump power dependence on fwhm of I_2, as shown in Figure 4b. It is evident that the fwhm of I_2 becomes narrower when the pump power approaches the ASE threshold, while the peak broadens when the excitation power is further increased, which is due to the multiple phonon broadening as discussed above.

The performance of CdS nanobelt optoelectronic devices also depends on the temperature. This is demonstrated by the temperature-dependent change of both the fwhm and the position of I_2, as shown in Figure 5. Here we had used a pump power (32 μW) that is beyond the ASE threshold to monitor the redistribution of bound exciton complexes during ASE at different temperatures. The red shift of the peak position at higher temperature follows the semiempirical theory known as the Varshni effect.[67] The fwhm, however, showed a nonmonotonous behavior as a function of temperature, which exhibits a dip at 100 K. Two possible processes (exciton−phonon interaction and the exciton−exciton interaction) are brought to provide an explanation. Agarwal *et al.*[68] found that exciton−exciton interaction is critical for lasing up to 70 K, while the exciton LO phonon process dominates at higher temperature. It will be shown later that the decay time of the ASE is invariant with temperature (Figure 6b), within the temporal resolution of the streak camera. This means that the exciton−exciton

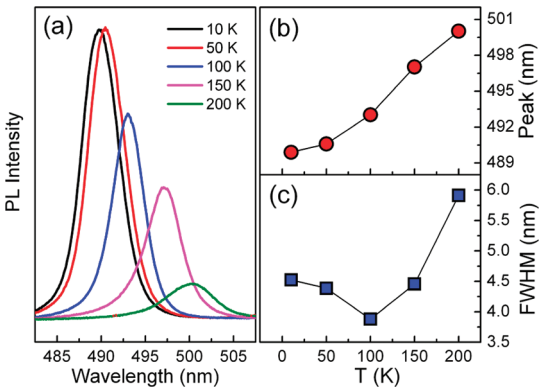

Figure 5. (a) Temperature-dependent PL intensity from CdS nanobelts following 470 nm excitation at 32 μW. (b) PL peak position and (c) fwhm of I_2 as a function of temperature.

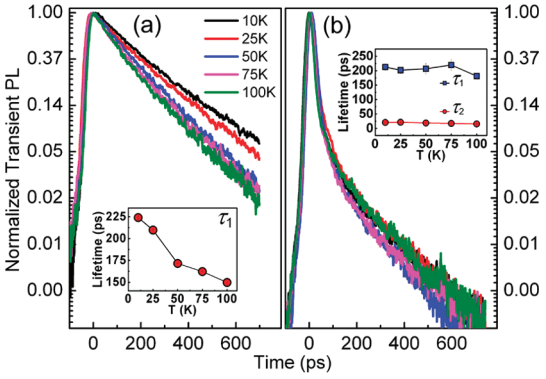

Figure 6. Temperature-dependent transient PL decay from band-edge bound exciton complexes in CdS nanobelts (a) at low excitation power of 2 μW and (b) at higher excitation power of 20 μW. The decay constants were extracted as a function of temperature as shown in the insets.

interaction responsible for the ASE mechanism is the same throughout different temperatures. At temperatures higher than 50 K, phonon absorption starts to play a role in assisting the nonradiative recombination channel as shown in the decrease of PL intensity in Figure 5a. This additional channel would lead to less carriers being involved in the ASE process. In the context of the state-filling effect, this dictates the line narrowing at 100 K. Beyond this temperature, however, the usual multiple phonon coupling and thermal broadening dominate, leading to the net broadening of the peak fwhm.

Time-Resolved Spectroscopy of Exciton Dynamics. The emergence of ASE and the dynamics of DAP emission processes are monitored with time-resolved PL as a function of pump power. Figure 4c shows the normalized I_2 decay at 10 K with 470 nm excitation. To evaluate the recombination lifetimes, the data were fitted by the biexponential decay function as follows:

$$A(t) = A_1\exp(-t/\tau_1) + A_2\exp(-t/\tau_2) \quad (2)$$

At a low pump power (below 2 μW), I_2 is dominated by a monoexponential decay ($\tau_1 \sim 250$ ps). This dynamics

reflects the intrinsic single exciton decay lifetime. However, at higher pump power over the ASE threshold (5 μW), the overall emission decay becomes much faster with the appearance of a second shorter lifetime ($\tau_2 \sim 20$ ps). This is consistent with the opening up of additional relaxation pathways corresponding to an increase in multiexciton interactions.

The PL lifetime measured by time-resolved PL consists of two contributions, radiative channel τ_{rad} and nonradiative τ_{nonrad} pathways. Overall, the lifetime measured by PL can be expressed as follows:

$$\frac{1}{\tau_{PL}} = \frac{1}{\tau_{rad}} + \frac{1}{\tau_{nonrad}} \quad (3)$$

The new decay channel could come from radiative part due to ASE and/or nonradiative part due to Auger process. The dimensions of our CdS samples are much larger than the exciton Bohr radius of approximately 2.8 nm for CdS.[20] Hence, the Auger recombination rates are effectively suppressed in this bulk-like system.[69] The strongly reduced Auger decay rates lead to increased optical gain lifetime and hence efficient light amplification.[70] While pump fluence is increased, PL intensity increases rapidly together with the emergence of a second PL lifetime τ_2 on the scale of 20 ps, which suggests the occurrence of ASE. Although we cannot decouple the radiative and the nonradiative rates in τ_2, we can deduce from Figure 6 that the nonradiative recombination rates (due to Auger recombination) are suppressed with the dominant contribution arising from the radiative process (*i.e.*, ASE) leading to a net superlinear increase of I_2 as a function of pump power, as shown in Figure 4b. It should be highlighted that different groups reported different τ_{PL} values ranging from several picoseconds to hundreds of picoseconds.[13,19,20] Henry *et al.* showed that the decay time constant of I_2 is about 500 ps,[24] while Dagenais *et al.* suggested that the lifetime is approximately 135 ps.[71] There have been limited reports on the ASE of CdS nanobelts for comparison. Nonetheless, τ_2, which is on the scale of 20 ps, is in agreement with the reports of ASE in ZnO.[68,72,73]

To further elucidate the effects of temperature on the decay lifetimes τ_1 and τ_2, we carried out temperature-dependent time-resolved PL measurements of the CdS nanobelts with 470 nm excitation pulses at two different pump powers, as shown in Figure 6a,b. At low pump power (2 μW, Figure 6a), the increase in temperature promotes the nonradiative relaxation process of I_2 emission, leading to faster time constant τ_1. The rate of this process can be described by the thermal activation energy in the Boltzmann distribution[74]

$$\frac{1}{\tau_{nonrad}(T)} = \frac{1}{\tau_{nonrad}(T=0)} e^{-E_a/k_B T} \quad (4)$$

where E_a is the activation energy for a nonradiative process. From eqs 3 and 4, we can see that the measured decay time constant decreases as the temperature increases, which is consistent with our experimental observations. In contrast, at high pump power (20 μW) exceeding the ASE threshold, both time constants (τ_1 and τ_2) are invariable with temperature, as shown in Figure 6b. It is likely that, at high pump fluence, there is a local laser heating generating a thermal bath, which screens the excitons from the variation of the surrounding temperature, resulting in the insensitivity of the τ_1 lifetime to changes of external temperatures. For τ_2, the radiative process (*i.e.*, ASE) has a larger rate constant than that for phonon emission; therefore, it can effectively compete with the phonon effects. Agarwal *et al.* also found that the dominant lasing line does not vary strongly with temperature as we have observed here for the evolution of excitons.[68]

For the DAP emission, the energy of the Hopfield-type donor and acceptor pair can be expressed as

$$E_{DAP}(r) = E_g - (E_D + E_A) + \frac{e^2}{4\pi\varepsilon\varepsilon_0 r} \quad (5)$$

where E_g is the band gap, while E_D and E_A are the activation energies of donor and acceptor, respectively.[75] The last term is the Coulomb energy between the donor and the acceptor, separated by a distance r. To give a good estimate, the donor−acceptor Coulomb interaction was calculated from the donor-to-acceptor transition energy ($E_g - E_D - E_A = 2.42$ eV) and the peak position of the zero phonon DAP emission (at 2.34 eV). The value for the Coulomb energy ($e^2/4\pi\varepsilon\varepsilon_0 r$) is approximately 80 meV. Using the dielectric constant $\varepsilon = 8.9$ of CdS, the estimated distance between the related donor and acceptor is about 20 Å, which is in the range of 3−5 times of CdS lattice constants and similar to the exciton Bohr radius. This suggests that the donors and the acceptors are rather localized in nature. Upon higher pump power, the number of occupied donor and acceptor centers increases and therefore their ensemble average distance r decreases, leading to a blue shift of the DAP emission. On the contrary, even though the pumping power is almost 4 times higher than that for I_2, there is still no wavelength shift (Figure 7b), and this reflects the saturation of DAP levels. As stated previously, saturation is due to the effect of limited cadmium vacancies in our samples. On the other hand, the photon energy of DAP also depends on the particular donor−acceptor pair distance as shown in eq 5. DAP distance determines the donor−acceptor wave function overlaps which dictate the time constants of particular DAP recombination. The closer they are, the shorter are their recombination lifetimes, which is clearly demonstrated by time-resolved measurements of the DAP PL peak (Figure 7c). Figure 7c displays three emission decays centered at the three different wavelengths of the zero phonon DAP PL spectrum (three arrows in Figure 7b). It is clear that closer

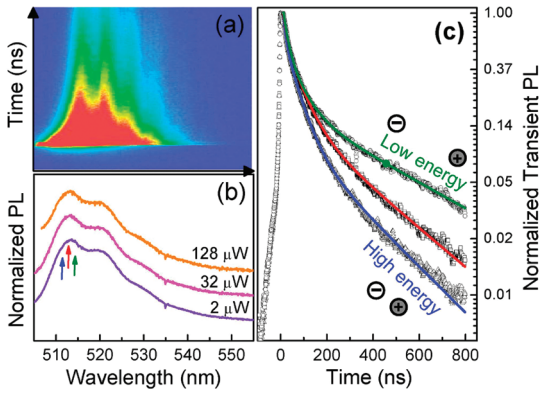

Figure 7. (a) Streak camera image showing the time-resolved PL emission of the DAP peaks. (b) Time-integrated PL spectra (normalized and shifted upward for clarity) of CdS nanobelts at 10 K with (470 nm, 150 fs, 1 kHz, 200 μm) an excitation power of 2, 32, and 128 μW. The colored arrows indicate the positions where the time-resolved PL dynamics shown in (c) were extracted. (c) Normalized transient PL decay dynamics of the DAP emission at three different wavelengths. Their fitting parameters are given in Table 1.

TABLE 1. Fitting Parameters for DAP Decay Curves (from top to bottom) in Figure 7c

decay constant	τ_{1DAP} (ns)	τ_{2DAP} (ns)
top	365 ± 3	39 ± 1
medium	236 ± 2	43 ± 1
bottom	195 ± 2	41 ± 1

donor–acceptor pairs (more energetic) undergo faster radiative recombination rates. The biexponential fitting in Figure 7c would just provide representative time constants for the DAP decay dynamics. The fitting parameters are listed in Table 1. The shorter lifetimes of the two constants are likely to arise from multiexciton interaction in DAP level, while the longer ones are related to the intrinsic DAP exciton recombination. An accurate description of the decay requires detailed knowledge of the donor–acceptor wave functions, which may not follow the simple hydrogenic orbitals. It is worthwhile to note that the longest decay lifetime for the DAP recombination is on the scale of several hundred nanoseconds and is much larger than I_2 (at least 3 orders). Although the localization of excitons could increase the lifetime, the extremely long decay time compared with I_2 may have other implications. One probable reason could be attributed to the intersystem crossing from the singlet states to triplet states. Usually the weak singlet–triplet splitting occurs in the CdS crystal with an energy splitting of approximately 2.2 meV,[76] which will increase the probability for excitons relaxing into the triplet states and emit the phosphorescence.[77] As seen from our calculations, the energy level of the cadmium vacancy shows a fairly good agreement with the energy difference between the valence band and the acceptor level. In addition, that level is also spin-polarized (Figure 3a), which will enhance the probability of spin-flip from the singlet to triplet state following photoexcitation.

CONCLUSION

Through first principle calculations and optical spectroscopy techniques, we show that the optical properties of CdS nanobelts are determined by the presence of intrinsic point defects, particularly the sulfur vacancy (donor) and the spin-polarized cadmium vacancy (acceptor). Our results suggest that these two vacancy states facilitate the formation of neutral donor bound excitons (I_2) with a fast decay dynamics on the order of tens to hundreds of picoseconds and a donor–acceptor pair (DAP) exciton complex with a much slower decay process on the order of hundreds of nanoseconds. The presence of Cd vacancy defects in CdS nanobelts does not affect the ASE process because the Cd vacancy state can easily be saturated at high photoexcitation power due to their slow recombination lifetime. Dynamic competition between I_2 and DAP has been identified, which suggests that compensation of acceptor level is the prerequisite to achieve ASE. The strongly reduced Auger decay rates lead to population inversion developed between donor level and valence level, resulting in ASE. Our results suggest the promise of engineering the luminescent properties in terms of both energy and lifetime of nanomaterials by controlling the species of defects.

EXPERIMENTAL SECTION

CdS Nanobelt Synthesis. Our samples were synthesized using a home-built vapor transport chemical vapor deposition system. In brief, CdS powder (99.995%) from Sigma-Aldrich was used as a precursor contained in a quartz boat, which was put into the center of the quartz tube. A silicon substrate was then put into the downstream. The tube was purged with a flow of Ar/5%H_2 to evacuate first, and then the furnace was heated to 670 °C with the carrier gas Ar flowing at a rate of 50 sccm for 30 min.

Steady-State Spectroscopy. A 325 nm He–Cd laser was chosen as an excitation wavelength in PL experiments. For the low-temperature measurement, a closed cycle refrigerated cryostat was used. The diffuse reflectance spectroscopy was conducted in a UV–vis–IR spectrometer (PerkinElmer, lambda 950) with a 150 mm integrating sphere detector.

Time-Resolved PL. Excitation pulses were generated from an optical parametric amplifier (TOPAS, Light Conversion Ltd.) that was pumped by a 1 kHz, 150 fs Ti:sapphire regenerative amplifier (Regen, Coherent, Inc.). The PL emission was collected in a standard backscattering geometry and dispersed by a 0.25 m DK240 spectrometer with a 150 g/mm grating. The PL signal was time-resolved using an Optronis Optoscope streak camera system which has an ultimate temporal resolution of 6 ps. For the data presented in the various time windows, the

streak camera has an effective temporal resolution of 10 ps for the band-edge transient PL and 10 ns for the defect emission.

Morphology and Crystallinity Characterizations. The as-grown nanobelts were characterized by X-ray diffraction (XRD, Bruker D8 Advanced Diffractometer with Cu Kα = 0.15419 nm), field emission scanning electron microscopy (FESEM, JEOL-7001F), transmission electron microscopy, selected area electron diffraction, and high-resolution transmission electron microscopy (HRTEM, JEOL JEM-2010).

Acknowledgment. Q.X. acknowledges strong support from Singapore National Research Foundation through NRF fellowship grant (NRF-RF2009-06), start-up grant support (M58113004), and New Initiative Fund (M58110100) from Nanyang Technological University (NTU). This work was also supported in part by the following research grants: an NTU start-up grant (M58110068), an Academic Research Fund (AcRF) Tier 1-RG 49/08 (M52110082); a Science and Engineering Research Council (SERC) Grant 042 101 0014, and an NRF Competitive Research Program (Grant No. NRF-G-CRP 2007-05).

REFERENCES AND NOTES

1. Bierman, M. J.; Lau, Y. K.; Kvit, A. V.; Schmitt, A. L.; Jin, S. Dislocation-Driven Nanowire Growth and Eshelby Twist. *Science* **2008,** *320*, 1060–1063.
2. Morin, S. A.; Bierman, M. J.; Tong, J.; Jin, S. Mechanism and Kinetics of Spontaneous Nanotube Growth Driven by Screw Dislocations. *Science* **2010,** *328*, 476–480.
3. Li, X.; Wang, X.; Xiong, Q.; Eklund, P. C. Mechanical Properties of ZnS Nanobelts. *Nano Lett.* **2005,** *5*, 1982–1986.
4. Xiong, Q.; Chen, G.; Acord, J. D.; Liu, X.; Zengel, J. J.; Gutierrez, H. R.; Redwing, J. M.; Voon, L. C. L. Y.; Lassen, B.; Eklund, P. C. Optical Properties of Rectangular Cross-Sectional ZnS Nanowires. *Nano Lett.* **2004,** *4*, 1663–1668.
5. Adu, K. W.; Xiong, Q.; Gutierrez, H. R.; Chen, G.; Eklund, P. C. Raman Scattering as a Probe of Phonon Confinement and Surface Optical Modes in Semiconducting Nanowires. *Appl. Phys. A* **2006,** *85*, 287–297.
6. Xiong, Q.; Wang, J.; Reese, O.; Voon, L. C. L. Y.; Eklund, P. C. Raman Scattering from Surface Phonons in Rectangular Cross-Sectional W-ZnS Nanowires. *Nano Lett.* **2004,** *4*, 1991–1996.
7. Duan, X.; Huang, Y.; Agarwal, R.; Lieber, C. M. Single-Nanowire Electrically Driven Lasers. *Nature* **2003,** *421*, 241–245.
8. Fan, Z.; Razavi, H.; Do, J.; Moriwaki, A.; Ergen, O.; Chueh, Y. L.; Leu, P. W.; Ho, J. C.; Takahashi, T.; Reichertz, L. A. Three-Dimensional Nanopillar-Array Photovoltaics on Low-Cost and Flexible Substrates. *Nat. Mater.* **2009,** *8*, 648–653.
9. Ma, R. M.; Dai, L.; Huo, H. B.; Xu, W. J.; Qin, G. G. High-Performance Logic Circuits Constructed on Single CdS Nanowires. *Nano Lett.* **2007,** *7*, 3300–3304.
10. Li, L.; Wu, P.; Fang, X.; Zhai, T.; Dai, L.; Liao, M.; Koide, Y.; Wang, H.; Bando, Y.; Golberg, D. Single-Crystalline CdS Nanobelts for Excellent Field-Emitters and Ultrahigh Quantum-Efficiency Photodetectors. *Adv. Mater.* **2010,** *22*, 3161–3165.
11. Pan, A.; Liu, D.; Liu, R.; Wang, F.; Zhu, X.; Zou, B. Optical Waveguide through CdS Nanoribbons. *Small* **2005,** *1*, 980–983.
12. Oulton, R. F.; Sorger, V. J.; Zentgraf, T.; Ma, R. M.; Gladden, C.; Dai, L.; Bartal, G.; Zhang, X. Plasmon Lasers at Deep Subwavelength Scale. *Nature* **2009,** *461*, 629–632.
13. Puthussery, J.; Lan, A.; Kosel, T. H.; Kuno, M. Band-Filling of Solution-Synthesized CdS Nanowires. *ACS Nano* **2008,** *2*, 357–367.
14. Chestnoy, N.; Harris, T. D.; Hull, R.; Brus, L. E. Luminescence and Photophysics of Cadmium Sulfide Semiconductor Clusters: The Nature of the Emitting Electronic State *J. Phys. Chem.* **1986,** *90*, 3393–3399.
15. Wang, C.; Ip, K. M.; Hark, S. K.; Li, Q. Structure Control of CdS Nanobelts and Their Luminescence Properties. *J. Appl. Phys.* **2005,** *97*, 054303.
16. Ip, K. M.; Wang, C. R.; Li, Q.; Hark, S. K. Excitons and Surface Luminescence of CdS Nanoribbons. *Appl. Phys. Lett.* **2004,** *84*, 795–797.
17. Gao, T.; Wang, T. Catalyst-Assisted Vapor−Liquid−Solid Growth of Single-Crystal CdS Nanobelts and Their Luminescence Properties. *J. Phys. Chem. B* **2004,** *108*, 20045–20049.
18. Wang, Z. Q.; Gong, J. F.; Duan, J. H.; Huang, H. B.; Yang, S. G.; Zhao, X. N.; Zhang, R.; Du, Y. W. Direct Synthesis and Characterization of CdS Nanobelts. *Appl. Phys. Lett.* **2006,** *89*, 033102.
19. Hoang, T. B.; Titova, L. V.; Jackson, H. E.; Smith, L. M.; Yarrison-Rice, J. M.; Lensch, J. L.; Lauhon, L. J. Temperature Dependent Photoluminescence of Single CdS Nanowires. *Appl. Phys. Lett.* **2006,** *89*, 123123.
20. Titova, L. V.; Hoang, T. B.; Jackson, H. E.; Smith, L. M.; Yarrison-Rice, J. M.; Lensch, J. L.; Lauhon, L. J. Low-Temperature Photoluminescence Imaging and Time-Resolved Spectroscopy of Single CdS Nanowires. *Appl. Phys. Lett.* **2006,** *89*, 053119.
21. Zeng, H.; Duan, G.; Li, Y.; Yang, S.; Xu, X.; Cai, W. Blue Luminescence of ZnO Nanoparticles Based on Non-equilibrium Processes: Defect Origins and Emission Controls. *Adv. Funct. Mater.* **2010,** *20*, 561–572.
22. Ischenko, V.; Polarz, S.; Grote, D.; Stavarache, V.; Fink, K.; Driess, M. Zinc Oxide Nanoparticles with Defects. *Adv. Funct. Mater.* **2005,** *15*, 1945–1954.
23. Henry, C. H.; Faulkner, R. A.; Nassau, K. Donor−Acceptor Pair Lines in Cadmium Sulfide. *Phys. Rev.* **1969,** *183*, 798–806.
24. Henry, C. H.; Nassau, K. Lifetimes of Bound Excitons in CdS. *Phys. Rev. B* **1970,** *1*, 1628–1634.
25. Henry, C. H.; Nassau, K.; Shiever, J. W. Double-Donor−Acceptor Pair Lines and the Chemical Identification of the I1 Lines in CdS. *Phys. Rev. Lett.* **1970,** *24*, 820–822.
26. Henry, C. H.; Nassau, K.; Shiever, J. W. Optical Studies of Shallow Acceptors in CdS and CdSe. *Phys. Rev. B* **1971,** *4*, 2453–2463.
27. Thomas, D. G.; Hopfield, J. J. Optical Properties of Bound Exciton Complexes in Cadmium Sulfide. *Phys. Rev.* **1962,** *128*, 2135–2148.
28. Christmann, M. H.; Dierssen, G. H.; Salmon, O. N.; Taylor, A. L.; Thom, W. H. Native Defect Changes in CdS Single Crystal Platelets Induced by Vacuum Heat Treatments at Temperatures up to 600 °C. *J. Phys. Chem. Solids* **1975,** *36*, 1371–1374.
29. Thomas, D. G.; Hopfield, J. J. Bound Exciton Complexes. *Phys. Rev. Lett.* **1961,** *7*, 316–319.
30. Klingshirn, C. F. *Semiconductor Optics*; Springer-Verlag: Berlin, 2007.
31. Nobbs, J. H. Kubelka-Munk Theory and the Prediction of Reflectance. *Rev. Prog. Color.* **1985,** *15*, 66–75.
32. Yu, Z.; Li, J.; O'Connor, D. B.; Wang, L. W.; Barbara, P. F. Large Resonant Stokes Shift in CdS Nanocrystals. *J. Phys. Chem. B* **2003,** *107*, 5670–5674.
33. Yang, B.; Schneeloch, J. E.; Pan, Z.; Furis, M.; Achermann, M. Radiative Lifetimes and Orbital Symmetry of Electronic Energy Levels of CdS Nanocrystals: Size Dependence. *Phys. Rev. B* **2010,** *81*, 073401.
34. Nirmal, M.; Norris, D. J.; Kuno, M.; Bawendi, M. G.; Efros, A. L.; Rosen, M. Observation of the "Dark Exciton" In CdSe Quantum Dots. *Phys. Rev. Lett.* **1995,** *75*, 3728–3731.
35. Xiao, Q.; Xiao, C. Surface-Defect-States Photoluminescence in CdS Nanocrystals Prepared by One-Step Aqueous Synthesis Method. *Appl. Surf. Sci.* **2009,** *255*, 7111–7114.
36. Imada, A.; Ozaki, S.; Adachi, S. Photoreflectance Spectroscopy of Wurtzite CdS. *J. Appl. Phys.* **2002,** *92*, 1793–1798.
37. Satoru, S. Photoluminescence, Reflectance and Photoreflectance Spectra in CdS Epilayers on Si(111) Substrates. *Jpn. J. Appl. Phys.* **2005,** *44*, 5913–5917.
38. Seto, S.; Kuroda, T.; Suzuki, K. Defect-Related Emission in CdS Films Grown Directly on Hydrogen-Terminated Si (111) Substrates. *Phys. Status Solidi C* **2006,** *3*, 803–806.
39. Chen, R.; Li, D.; Liu, B.; Peng, Z.; Gurzadyan, G. G.; Xiong, Q.; Sun, H. Optical and Excitonic Properties of Crystalline ZnS

Nanowires: Toward Efficient Ultraviolet Emission at Room Temperature. *Nano Lett.* **2010,** *10*, 1897–1899.
40. Reynolds, D. C.; Collins, T. C. Donor–Acceptor Pair Recombination Spectra in Cadmium Sulfide Crystals. *Phys. Rev.* **1969,** *188*, 1267–1271.
41. Gutowski, J.; Broser, I. Electronic and Vibronic States of the Acceptor-Bound-Exciton Complex (A0,X) in CdS. III. High-Density Electronic Resonant Raman Scattering at the (A0, X) Complex. *Phys. Rev. B* **1985,** *31*, 3621.
42. Debernardi, A.; Pyka, N. M.; Gobel, A.; Ruf, T.; Lauck, R.; Kramp, S.; Cardona, M. Lattice Dynamics of Wurtzite CdS: Neutron Scattering and *Ab-Initio* Calculations. *Solid State Commun.* **1997,** *103*, 297–301.
43. Beserman, R. Zone Edge Phonons in $CdS_{1-x}Se_x$. *Solid State Commun.* **1977,** *23*, 323–327.
44. Ekimov, A. I.; Kudryavtsev, I. A.; Ivanov, M. G.; Efros, A. L. Spectra and Decay Kinetics of Radiative Recombination in CdS Microcrystals. *J. Lumin.* **1990,** *46*, 83–95.
45. Moroz, M.; Brada, Y.; Honig, A. Bound Donor–Acceptor Edge Luminescence Line Shapes in CdS. *Solid State Commun.* **1983,** *47*, 115–120.
46. Zhao, H.; Kalt, H. Energy-Dependent Huang-Rhys Factor of Free Excitons. *Phys. Rev. B* **2003,** *68*, 125309.
47. Broser, I.; Gutowski, J.; Riedel, R. Excitation Spectroscopy of the Donor–Acceptor-Pair Luminescence in CdS. *Solid State Commun.* **1984,** *49*, 445–449.
48. Goto, F.; Shirai, K.; Ichimura, M. Defect Reduction in Electrochemically Deposited CdS Thin Films by Annealing in O_2. *Sol. Energy Mater. Sol. Cells* **1998,** *50*, 147–154.
49. Dovesi, R.; Civalleri, B.; Orlando, R.; Roetti, C.; Saunders, V. R. *Ab Initio* Quantum Simulation in Solid State Chemistry. *Rev. Comput. Chem.* **2005,** *21*, 1.
50. Collins, R. J. Mechanism and Defect Responsible for Edge Emission in CdS. *J. Appl. Phys.* **1959,** *30*, 1135.
51. Handelman, E. T.; Thomas, D. G. The Effects of Low Temperature Heat Treatments on the Conductivity and Photoluminescence of CdS. *J. Phys. Chem. Solids* **1965,** *26*, 1261–1267.
52. Wang, Y.; Meng, G.; Zhang, L.; Liang, C.; Zhang, J. Catalytic Growth of Large-Scale Single-Crystal CdS Nanowires by Physical Evaporation and Their Photoluminescence. *Chem. Mater.* **2002,** *14*, 1773–1777.
53. Kar, S.; Chaudhuri, S. Cadmium Sulfide One-Dimensional Nanostructures: Synthesis, Characterization and Application. *Synth. React. Inorg., Met.-Org. Chem.* **2006,** *36*, 289–312.
54. Zhai, T.; Fang, X.; Bando, Y.; Golberg, D. One-Dimensional CdS Nanostructures: Synthesis, Properties, and Applications. *Nanoscale* **2010,** *2*, 168–187.
55. Shiraki, Y.; Shimada, T.; Komatsubara, K. F. Optical Studies of Deep Center Luminescence in CdS. *J. Appl. Phys.* **1974,** *45*, 3554–3561.
56. Chen, K. T.; Zhang, Y.; Egarievwe, S. U.; George, M. A.; Burger, A.; Su, C. H.; Sha, Y. G.; Lehoczky, S. L. Post-Growth Annealing of CdS Crystals Grown by Physical Vapor Transport. *J. Cryst. Growth* **1996,** *166*, 731–735.
57. Magde, D.; Mahr, H. Exciton–Exciton Interaction in CdS, CdSe, and ZnO. *Phys. Rev. Lett.* **1970,** *24*, 890–893.
58. Wiersma, D. S. The Physics and Applications of Random Lasers. *Nat. Phys.* **2008,** *4*, 359–367.
59. Klimov, V. I.; Mikhailovsky, A. A.; Xu, S.; Malko, A.; Hollingsworth, J. A.; Leatherdale, C. A.; Eisler, H. J.; Bawendi, M. G. Optical Gain and Stimulated Emission in Nanocrystal Quantum Dots. *Science* **2000,** *290*, 314–317.
60. Huang, M. H.; Mao, S.; Feick, H.; Yan, H.; Wu, Y.; Kind, H.; Weber, E.; Russo, R.; Yang, P. Room-Temperature Ultraviolet Nanowire Nanolasers. *Science* **2001,** *292*, 1897–1899.
61. Pan, H.; Xing, G.; Ni, Z.; Ji, W.; Feng, Y. P.; Tang, Z.; Chua, D. H. C.; Lin, J.; Shen, Z. Stimulated Emission of CdS Nanowires Grown by Thermal Evaporation. *Appl. Phys. Lett.* **2007,** *91*, 193105.
62. Pan, A.; Liu, R.; Wang, F.; Xie, S.; Zou, B.; Zacharias, M.; Wang, Z. L. High-Quality Alloyed CdS_xSe_{1-x} Whiskers as Waveguides with Tunable Stimulated Emission. *J. Phys. Chem. B* **2006,** *110*, 22313–22317.
63. Chen, R.; Bakti Utama, M. I.; Peng, Z.; Peng, B.; Xiong, Q.; Sun, H. Excitonic Properties and near Infrared Coherent Random Lasing in Vertically Aligned CdSe Nanowires. *Adv. Mater.* **2011,** *23*, 1404–1408.
64. Klimov, V. I.; Ivanov, S. A.; Nanda, J.; Achermann, M.; Bezel, I.; McGuire, J. A.; Piryatinski, A. Single-Exciton Optical Gain in Semiconductor Nanocrystals. *Nature* **2007,** *447*, 441–446.
65. Schmitt-Rink, S.; Chemla, D. S.; Miller, D. A. B. Linear and Nonlinear Optical Properties of Semiconductor Quantum Wells. *Adv. Phys.* **1989,** *38*, 89–188.
66. Klingshirn, C.; Fallert, J.; Zhou, H.; Sartor, J.; Thiele, C.; Maier-Flaig, F.; Schneider, D.; Kalt, H. 65 Years of ZnO Research-Old and Very Recent Results. *Phys. Status Solidi B* **2010,** *247*, 1424–1447.
67. Varshni, Y. P. Temperature Dependence of the Energy Gap in Semiconductors. *Physica* **1967,** *34*, 149–154.
68. Agarwal, R.; Barrelet, C. J.; Lieber, C. M. Lasing in Single Cadmium Sulfide Nanowire Optical Cavities. *Nano Lett.* **2005,** *5*, 917–920.
69. Klimov, V. I.; Mikhailovsky, A. A.; McBranch, D. W.; Leatherdale, C. A.; Bawendi, M. G. Quantization of Multiparticle Auger Rates in Semiconductor Quantum Dots. *Science* **2000,** *287*, 1011–1013.
70. Htoon, H.; Hollingsworth, J. A.; Dickerson, R.; Klimov, V. I. Effect of Zero- to One-Dimensional Transformation on Multiparticle Auger Recombination in Semiconductor Quantum Rods. *Phys. Rev. Lett.* **2003,** *91*, 227401.
71. Dagenais, M.; Sharfin, W. F. Linear- and Nonlinear-Optical Properties of Free and Bound Excitons in CdS and Applications in Bistable Devices. *J. Opt. Soc. Am. B* **1985,** *2*, 1179–1187.
72. Zou, B.; Liu, R. B.; Wang, F.; Pan, A.; Cao, L.; Wang, Z. L. Lasing Mechanism of ZnO Nanowires/Nanobelts at Room Temperature. *J. Phys. Chem. B* **2006,** *110*, 12865–12873.
73. Johnson, J. C.; Knutsen, K. P.; Yan, H.; Law, M.; Zhang, Y.; Yang, P.; Saykally, R. J. Ultrafast Carrier Dynamics in Single ZnO Nanowire and Nanoribbon Lasers. *Nano Lett.* **2004,** *4*, 197–204.
74. Kim, D.; Mishima, T.; Tomihira, K.; Nakayama, M. Temperature Dependence of Photoluminescence Dynamics in Colloidal CdS Quantum Dots. *J. Phys. Chem. C* **2008,** *112*, 10668–10673.
75. Shiraki, Y.; Shimada, T.; Komatsubara, K. F. Edge Emissions of Ion-Implanted CdS. *J. Phys. Chem. Solids* **1977,** *38*, 937–941.
76. Oka, Y.; Kushida, T. Mixing of Singlet and Triplet Exciton States in Highly Excited CdS. *Solid State Commun.* **1974,** *15*, 1571–1575.
77. Mueller, M. L.; Yan, X.; McGuire, J. A.; Li, L. Triplet States and Electronic Relaxation in Photoexcited Graphene Quantum Dots. *Nano Lett.* **2010,** 1530–1534.